Sub-decadal Volcanic Tsunamis Due to Submarine Trapdoor Faulting at Sumisu Caldera in the Izu–Bonin Arc

Osamu Sandanbata,[1,2,†] Shingo Watada,[1] Kenji Satake,[1] Hiroo Kanamori,[3] Luis Rivera,[4] and Zhongwen Zhan[3]

[1] Earthquake Research Institute, The University of Tokyo, Bunkyo, Tokyo, Japan.

[2] National Research Institute for Earth Science and Disaster Resilience, Tsukuba, Ibaraki, Japan.

[3] Seismological Laboratory, California Institute of Technology, Pasadena, CA 91125, USA.

[4] Université de Strasbourg, CNRS, ITES UMR 7063, Strasbourg F-67084, France.

Corresponding author: Osamu Sandanbata (osm3@bosai.go.jp)

† Current address: National Research Institute for Earth Science and Disaster Resilience, Tsukuba, Ibaraki, Japan.

Key Points:

- Large tsunamis are generated by moderate-sized volcanic earthquakes at a submarine caldera.
- Tsunami and seismic data indicate that abrupt inflation of the submarine caldera by trapdoor faulting causes large tsunamis.
- Continuous magma supply into the submarine caldera induces submarine trapdoor faulting on a decadal timescale.

Abstract

The main cause of tsunamis is large subduction zone earthquakes with seismic magnitudes $M_w >$ 7, but submarine volcanic processes can also generate tsunamis. At the submarine Sumisu caldera in the Izu–Bonin arc, moderate-sized earthquakes with $M_w < 6$ occur on a decadal timescale and cause meter-scale tsunamis. The source mechanism of the volcanic earthquakes is poorly understood. Here we use tsunami and seismic data for the recent 2015 event to show that abrupt inflation of the submarine caldera, with a large brittle rupture of the ring fault system due to overpressure in its magma reservoir, caused the earthquake and tsunami. This submarine trapdoor faulting mechanism can efficiently generate tsunamis due to the large, shallow, and complex rupture, but it inefficiently radiates long-period seismic waves. Similar seismic radiation patterns and tsunami waveforms due to repeated earthquakes indicate that continuous magma supply into the caldera induces quasi-regular trapdoor faulting. This mechanism of tsunami generation by submarine trapdoor faulting underscores the need to monitor submarine calderas for robust assessment of tsunami hazards.

Plain Language Summary

Tsunamis are mainly caused by large submarine earthquakes, but submarine volcanic processes can also trigger tsunamis. Anomalous tsunami waves have been generated every decade by moderate-sized volcanic earthquakes at a submarine volcano with a caldera structure, called the Sumisu caldera. Despite the moderate earthquake size, the maximum wave heights of the tsunamis were about a meter, and their source mechanism has been controversial. In this study, we used tsunami and ground motion data for a recent earthquake to show that its submarine caldera regularly and abruptly causes brittle fracturing of its intra-caldera fault system in

response to overpressurization of magma accumulating in the underlying magma chamber, which leads to large inflation of the caldera. Our discovery of this atypical source mechanism for tsunami generation suggests it is important to monitor active submarine calderas when assessing tsunami hazards.

1 Introduction

Large earthquakes in subduction zones with seismic moment magnitudes $M_w > 7$ are the main causes of tsunamis, but other submarine geophysical processes, such as volcanism or landslides, can also trigger tsunamis (Kanamori, 1972; Paris, 2015; Satake, 2015; Ward, 2001). Given the latter typically do not involve significant seismic ground motions, the difficulty in forecasting tsunamis results in increased tsunami risk to coastal societies (Grilli et al., 2019; Hunt et al., 2021; Tappin et al., 1999; Walter et al., 2019). Unusual tsunamis have been reported for earthquakes generated at the Sumisu caldera (also known as Smith caldera), which is a submarine volcano with an 8 × 10 km caldera structure in the Izu–Bonin arc (Figure 1) (Shukuno et al., 2006; Tani et al., 2008). At the caldera, volcanic earthquakes with moderate seismic magnitudes (M_w 5.4–5.7) have occurred quasi-regularly in 1984, 1996, 2006, 2015, and 2018 (Figure 1b; Table S1), which are known as Torishima earthquakes (Fukao et al., 2018; Kanamori et al., 1993; Satake & Kanamori, 1991). The earthquake on 2 May 2015 (M_w 5.7) caused an unusually large tsunami with a maximum wave height of 1 m on Hachijojima Island, located 180 km north of the caldera (Figure 1c), although no ground shaking was felt on the island. The other four earthquakes also caused relatively large tsunamis with similar waveforms at many tide gauge stations (Figures 1d–e and S1). The five earthquakes were seismologically similar to each other, and all had a moment tensor with a large compensated-linear-vector-dipole (CLVD) component and a dominant tension axis in a nearly vertical direction (Figure 1b), which is often called a vertical-T CLVD earthquake (Shuler, Ekström, et al., 2013; Shuler, Nettles, et al., 2013).

Since the 1984 earthquake, various models have been proposed for this atypical earthquake mechanism and tsunami generation. These include dip slip on a curved ring fault system of a caldera, vertical opening of a shallow horizontal crack, and volume change (Ekström, 1994; Fukao et al., 2018; Kanamori et al., 1993; Satake & Kanamori, 1991). However, different interpretations can explain the moment tensors (Shuler, Ekström, et al., 2013), and no consensus on the earthquake mechanism has yet been reached, because of the inaccessibility of the submarine caldera. For the 2015 earthquake, the tsunami was recorded by high-quality ocean-bottom pressure (OBP) gauges of a temporary array and recently deployed tsunami observation networks to the south of Japan (Figure 1a). The obtained tsunami waveform and regional seismic data provide an opportunity to determine the mechanisms responsible for these anomalous volcanic earthquakes.

The objective of this study is to determine the source mechanism responsible for the volcanic earthquakes at Sumisu caldera. We initially conduct a preliminary analysis using only the tsunami waveform data to estimate the sea-surface disturbance due to the coseismic seafloor deformation. We then combine the tsunami and long-period seismic data to develop a source model that can quantitatively explain both datasets. Based the model, we discuss the source mechanism of the earthquakes, possible causes of the efficient tsunami excitation and its sub-decadal recurrence, and implications for the submarine volcanism of Sumisu caldera.

2 Data

2.1 Tsunami data

We use tsunami data recorded by 24 OBP gauges (Figure 1a) of the array off Aogashima Island, the Dense Oceanfloor Network system for Earthquakes and Tsunamis (DONET) system, the Deep Sea Floor Observatory (DSFO) off Muroto Cape, and the Deep-ocean Assessment and Reporting of Tsunamis (DART) system. We manually check the data quality (i.e., data gaps, spikes, or repeated values) near the arrival times of the tsunami signals and remove tidal trends by fitting polynomial functions. We apply a two-pass second-order low-pass Butterworth filter to the synthetic and observed waveforms. The cut-off frequencies are 0.0125, 0.0083, 0.0083, and 0.00667 Hz for stations from the array, DONET, DSFO, and DART, respectively, depending on the maximum depth along a source–station path, following the study (Sandanbata, Watada, et al., 2021).

2.2 Long-period seismic data

We use seismic data recorded by the BH channel (three components) of 36 regional stations (epicentral distance < 30°) of the F-net and Global Seismograph Network (GSN). The seismic stations are listed in Table S2. We remove the instrument response from the observed seismograms to obtain the displacement records, and apply a one-pass fourth-order band-pass Butterworth filter with corner frequencies of 0.004 and 0.0167 Hz (band-pass period = 60–250 s) using the W-phase package (Duputel et al., 2012; Hayes et al., 2009; Kanamori & Rivera, 2008).

3 Preliminary analysis: Estimation of the initial sea-surface displacement

As a preliminary step for the source modeling of the 2015 earthquake, we estimate the initial sea-surface displacement caused by the earthquake using a tsunami waveform inversion method. To compute synthetic tsunami waveforms, we first assume 113 unit sources of sea-surface displacement at 2-km intervals in a source area of 32 × 32 km around Sumisu caldera (Figure S2). Each unit source has a cosine-tapered shape (Hossen et al., 2015):

$$\eta^k(x, y) = 0.25 \times \left[1.0 + \cos\frac{\pi(x - x^k)}{L}\right] \times \left[1.0 + \cos\frac{\pi(y - y^k)}{L}\right], \quad (|x - x^k|, |y - y^k| \leq L) \tag{1}$$

where (x^k, y^k) is the central location in kilometers of the *k*th unit source ($k = 1, 2, \ldots, K$; here K = 113) with a source size of $2L$ (i.e., 4.0 km). The rise time for each unit source is 10 s, given that the earthquake source duration is 10 s as estimated by our moment tensor analysis (Text S1; Table S3).

We use simulation methods of tsunami propagation including the effects of the tsunami dispersion, the compressibility and the density stratification of seawater, and the elasticity of the Earth. For the short-period tsunami waveforms at the stations, except for 52404, we solve the linear Boussinesq equations (Peregrine, 1972) with the JAGURS code (Baba et al., 2015) and apply a phase correction to the short-period tsunamis (Sandanbata, Watada, et al., 2021). For the relatively long-period waveform at the distant station 52404 (located ~1,400 km from the epicenter), we solve the linear long-wave equations with the JAGURS code (Baba et al., 2015) and apply a phase correction for long-period tsunamis (Ho et al., 2017) to reduce the computational cost. In both cases, the computational time-step interval is 0.25 s. We use high-resolution bathymetric data (10 arcsec grid spacing) processed from the M7000 series for the area near Sumisu caldera and Aogashima Island, whereas we use JTOPO30 and GEBCO_2014 (30 arcsec grid spacing) for the other regions. When the tsunami wavelength is comparable or shorter than the water depth, the bottom pressure change becomes smaller than the static water pressure of the same height. To include this pressure reduction effect, we apply the Kajiura filter (Kajiura, 1963) to the wave-height field output for every 5.0 s and obtain the OBP change at the stations (Chikasada, 2019). We apply the same filter to the synthetic waveform of the OBP change as used for the OBP data. Hereafter, the tsunami waveforms are OBP waveforms (in the [cm H_2O] scale).

We then restore the synthetic tsunami waveforms from the *k*th unit source to the *j*th station ($j = 1, 2, \ldots, J$; here $J = 24$) as a matrix $g_j^k(t)$ and solve the observation equation with the damped least-squares method (pp. 695–699 in Aki & Richards [1980]):

$$\begin{bmatrix} \overline{\boldsymbol{d}} \\ \boldsymbol{0} \end{bmatrix} = \begin{bmatrix} \overline{\boldsymbol{g}} \\ \alpha \boldsymbol{I} \end{bmatrix} \boldsymbol{m}, \tag{2}$$

where $\overline{\boldsymbol{d}} = [w_1 d_1(t) \quad \cdots \quad w_J d_J(t)]^T$ is the column vector of the observed data $d_j(t)$ weighted by w_j at the *j*th station (Equation 3; see below), $\overline{\boldsymbol{g}} = \begin{bmatrix} w_1 g_1^1(t) & \cdots & w_1 g_1^K(t) \\ \vdots & \ddots & \vdots \\ w_J g_J^1(t) & \cdots & w_J g_J^K(t) \end{bmatrix}$ is the matrix $g_j^k(t)$ weighted by w_j, $\boldsymbol{m} = [m^1 \quad \cdots \quad m^K]^T$ is an unknown column vector of the weighting factors for the *k*th unit source, $\boldsymbol{I}$ is the identity matrix, and α is the damping parameter used to obtain a smooth model. We assume $\alpha = 2.0$. For normalization of the waveforms, we define the inverse root-mean-square (RMS) value w_j at each station (Ho et al., 2017):

$$\frac{1}{w_j} = \sqrt{\frac{\sum_{l=0}^{\gamma_j} \{d_j(t_l)\}^2}{\gamma_j}}, \tag{3}$$

where $d_j(t_l)$ is the tsunami waveform data for the jth station and γ_j is the number of the data points used for the analysis.

Consequently, we obtain an initial sea-surface displacement model, composed of a localized sea-surface uplift of about 1 m over the northeastern side of the caldera floor and smaller subsidence outside of the caldera rim (Figure 2a). This model reproduces the tsunami waveform data (Figure S3). A previous study (Fukao et al., 2018) proposed a symmetrical caldera floor uplift model surrounded by peripheral subsidence, but our tsunami waveform inversion using more OBP data with wider azimuthal coverage indicates that deformation is localized on the northeastern side of the caldera. To examine the robustness of the exterior subsidence, we estimate the initial sea-surface uplift model, without subsidence, by imposing a non-negative condition when solving Equation 2. The obtained uplift model, containing only a larger northeastern uplift, cannot reproduce the tsunami first motions with initial downswing signals of the relatively near-field stations in the northeastern direction (A01–10; Figure 2b). This result suggests that, during the earthquake, the exterior of the caldera subsided, at least on its northeastern side.

4 Source modeling of the 2015 earthquake: methodology

4.1 Hypothetical earthquake source mechanism

We next explore the source model of the 2015 earthquake by combining analyses of the tsunami and long-period seismic data. From the deformation pattern determined in the preliminary analysis (Section 3), we hypothesize that the source mechanism of *trapdoor faulting*, which can be represented by dip slip along a ring fault system and the opening and/or closure of a shallow horizontal crack (Figure 3a). This mechanism was first proposed for volcanic earthquakes at the subaerial caldera of Sierra Negra in the Galapagos Islands (Amelung et al., 2000). Previous studies have suggested that magma overpressure in a shallow sill-like reservoir pushed up a caldera block above the reservoir, which caused a large uplift near the reverse-slip ring fault in the caldera (Chadwick et al., 2006; Jónsson, 2009; Yun, 2007; Zheng et al., 2021), and that the seismic radiation was characterized by a vertical-T CLVD moment tensor (Sandanbata, Kanamori, et al., 2021; Shuler, Ekström, et al., 2013). The trapdoor faulting at Sumisu caldera is presumed to have generated asymmetric coseismic deformation (Section 3), with a vertical-T CLVD earthquake. Young lava domes located along a line forming an elliptic shape on the floor of Sumisu caldera (Tani et al., 2008) (Figure 1b) also indicate that a ring fault system is connected to a shallow reservoir filled with magma (Cole et al., 2005).

4.2 Tsunami waveform inversion for trapdoor faulting

We again use a tsunami waveform inversion method with the OBP data but this time for directly determining the trapdoor faulting motion, or spatial distribution of dip slip along the ring fault and vertical opening and/or closure of the horizontal crack. The inversion procedure for the trapdoor faulting motion is as follows.

We first assume the source structures are a ring fault and a horizontal crack beneath Sumisu caldera (Figure 3b). The ring fault extends from the seafloor to the edge of the horizontal crack with a uniform dip angle (Figure 1b). We discretize the structure with triangular source elements using the DistMesh code (Persson & Strang, 2004). We model a sub-fault of the ring fault by a rhomb shape composed two neighboring triangular source elements with the same dip and strike angles, and sub-crack of the horizontal crack by a triangular source element. We fix the midpoint of the ring fault segment to the northeastern corner of the caldera. To constrain the source geometry, we prepare tens of structures with three variable geometric parameters: (a) the depth of the horizontal crack (3 or 6 km); (b) the dip angle of the ring fault (70–90°); and (c) the arc length of the ring fault (one-third, two-third, and a full ring; Figure S4).

We then compute synthetic tsunami waveforms, or Green's functions G_{ij}, relating dislocations (i.e., dip slip of the sub-fault, and vertical opening of the sub-crack) of *i*th source element ($i = 1, 2, \dots, I$; I depends on source structures) to the tsunami waveform at the *j*th station with the following three steps. Firstly, we calculate the vertical seafloor displacement from a 1 m dislocation of each source element with the triangular dislocation method (Nikkhoo & Walter, 2015) and transform it into the sea-surface displacement by applying the Kajiura filter (Kajiura, 1963). We note that when the horizontal scale of the seafloor uplift is comparable to or smaller than the water depth, the vertical sea-surface displacement is smaller than the vertical seafloor displacement, which is in contrast to the pressure reduction from sea surface to seafloor (Section 3.1). We apply the Kajiura filter forward in the former case and backward in the latter case. For these computations, we assume a Poisson's ratio of 0.25 for the crust and a flat seafloor below a water layer at a depth of 800 m. We thus compute the sea-surface displacement from the *i*th source element $h_i(x, y)$. Secondly, the sea-surface displacement $h_i(x, y)$ is approximated by a linear combination of the unit sources $\eta^k(x, y)$, used in Section 3 (Equation 1; Figure S2):

$$h_i(x, y) \approx \sum_{k=1}^{K} m_i^k \eta^k(x, y), \tag{4}$$

where the weighting factors m_i^k are obtained by a least square adjustment of Equation 4. Thirdly, we obtain Green's functions relating the *i*th source element to the *j*th station by superimposing the synthetic tsunami waveforms from the *k*th unit sources $g_j^k(t)$ (Section 3) weighted by m_i^k, as follows:

$$G_{ij}(t) = \sum_{k=1}^{K} m_i^k g_j^k(t). \tag{5}$$

By reusing the synthetic tsunami waveforms computed in Section 3, we do not have to perform the tsunami waveform simulation, which significantly reduces the computational cost. Hence, we can efficiently assess inversions for tens of source structures, each of which consists of $I > 50$ source elements.

Using the Green's functions G_{ij}, we solve the observation equation with the damped least-squares method:

$$\begin{bmatrix} \bar{\boldsymbol{d}} \\ \boldsymbol{0} \end{bmatrix} = \begin{bmatrix} \bar{\boldsymbol{G}} \\ \beta \boldsymbol{I} \end{bmatrix} \boldsymbol{X}, \tag{6}$$

where $\bar{\boldsymbol{d}}$ is the column vector of the observed tsunami waveforms d_j normalized by w_j at the *j*th station (Equation 3). $\bar{\boldsymbol{G}} = \begin{bmatrix} w_1 G_{11}(t) & \cdots & w_1 G_{I1}(t) \\ \vdots & \ddots & \vdots \\ w_J G_{1J} & \cdots & w_J G_{IJ}(t) \end{bmatrix}$ is the matrix of the Green's functions G_{ij} normalized by w_j. $\boldsymbol{X} = [X_1 \quad \cdots \quad X_I]^T$ is an unknown column vector of dislocation amounts of the *i*th source element. β is the damping parameter for smoothing, which we set to 0.3. The inversion time windows include several wave crests and troughs. Thus, we obtain a source model for the trapdoor faulting on an assumed source structure.

To evaluate the model performance, we calculate the normalized root-mean-square (NRMS) misfit of the tsunami waveforms, which we term the tsunami waveform misfit:

$$\rho^t = \sqrt{\sum_j \left\| \boldsymbol{s}_j^t - \boldsymbol{d}_j^t \right\|^2 / \sum_j \left\| \boldsymbol{s}_j^t \right\|^2}, \tag{7}$$

where $\boldsymbol{d}_j^t$ and $\boldsymbol{s}_j^t$ are the column vector of the observed and synthetic tsunami waveforms of the model in inversion time window at the *j*th station, respectively. $\|\boldsymbol{s}\|$ is the L2 norm of data vector $\boldsymbol{s}$.

4.3 Computation of the long-period seismic waveforms

For validation of the source model inverted from the tsunami data, we compute the long-period seismic waveforms of the model and compare these with the long-period seismic data. Because the wave length of seismic data we use is much longer than the size of the caldera, the seismic source can be modeled by a point-source moment tensor. The total moment tensor $\boldsymbol{M}$ of the source model is calculated as:

$$\boldsymbol{M} = \boldsymbol{M}_{RF} + \boldsymbol{M}_{HC} = \sum \boldsymbol{m}_{RF}^p + \sum \boldsymbol{m}_{HC}^q, \quad (8)$$

where $\boldsymbol{M}_{RF}$ and $\boldsymbol{M}_{HC}$ are the moment tensors of the ring fault and horizontal crack, respectively, and $\boldsymbol{m}_{RF}^p$ and $\boldsymbol{m}_{HC}^q$ are the moment tensors of the *p*th sub-fault slip and *q*th sub-crack opening or closure, respectively (Figure S5a). The coordinate system is (r, θ, ϕ) for [up, south, east]. $\boldsymbol{m}_{RF}^p$ is computed from the slip amount and strike, dip, and rake (90°) angles of the *p*th sub-fault (Box 4.4 in Aki & Richards [1980]). The seismic moment is computed as $\mu \Delta u_p S_p$, where Δu_p and S_p are the slip amount and area, and μ is the rigidity, or Lamé's constant. $\boldsymbol{m}_{HC}^q$ is calculated as:

$$\boldsymbol{m}_{HC}^q = \begin{bmatrix} M_{rr} & M_{\theta r} & M_{\phi r} \\ M_{r\theta} & M_{\theta\theta} & M_{\phi\theta} \\ M_{r\phi} & M_{\theta\phi} & M_{\phi\phi} \end{bmatrix} = \Delta u_q \times S_q \times \begin{bmatrix} \lambda + 2\mu & 0 & 0 \\ 0 & \lambda & 0 \\ 0 & 0 & \lambda \end{bmatrix}, \quad (9)$$

where Δu_q and S_q are the opening amount and area of the *q*th sub-crack, respectively (Kawakatsu & Yamamoto, 2015). Lamé's constants λ and μ are assumed to be 29.90 and 31.85

GPa, respectively, based on the P- and S-wave velocities (V_p = 6.0 km/s and V_s = 3.5 km/s) and the density (ρ_0 = 2.6 × 10^3 kg/m^3) in the shallowest layer of the Earth model (Figure S5b). The scalar seismic moment of the moment tensor is $M_0 = \sqrt{\Sigma_{ij} M_{ij} M_{ij}/2}$ (pp. 166–167 in Dahlen & Tromp [1998]; Silver & Jordan, 1982), and the moment magnitude is $M_w = \frac{2}{3}(\log_{10} M_0 - 9.10)$, with M_0 in the [N m] scale (Hanks & Kanamori, 1979; Kanamori, 1977).

By assuming the moment tensor (Equation 8), we compute the long-period (60–250 s) seismic waveforms with the W-phase package (Duputel et al., 2012; Hayes et al., 2009; Kanamori & Rivera, 2008). We compute the Green's functions of the seismic waveforms for the one-dimensional crustal velocity model for Japan (Figure S5b) using the wavenumber integration method (Herrmann, 2013). We fix the centroid location at a depth of 2.5 km below the seafloor in the center of Sumisu caldera (140.053°E, 31.485°N). Both the half duration and centroid time shift are assumed to be 5 s, as obtained by our moment tensor analysis (Text S1; Table S3). We apply the same filter as used for the seismic data.

To evaluate the model performance, we calculate the NRMS misfit of the long-period seismic waveforms, which we term the seismic waveform misfit:

$$\rho^s = \sqrt{\Sigma_j \left\| \boldsymbol{s}_j^s - \boldsymbol{d}_j^s \right\|^2 / \Sigma_j \left\| \boldsymbol{s}_j^s \right\|^2}, \tag{10}$$

where $\boldsymbol{s}_j^s$ and $\boldsymbol{d}_j^s$ are the column vectors of the synthetic and observed seismic records at the jth channels, respectively. We set the time window to include the P, S, and surface waves.

5 Source modeling of the 2015 earthquake: Results

From the tsunami waveform inversion, we obtain tens of source models for the 2015 earthquake with different combinations of the three geometric source parameters (i.e., the depth of the horizontal crack and ring fault dip angle and arc length). An example is shown in Figure 3b. The patterns of trapdoor faulting motion determined by the tsunami waveform inversion are different depending on the depth of the horizontal crack, which allows us to estimate the source depth. When we assume the horizontal crack is at a depth of 6 km (Figure 4a), the motion of the ring fault changes from reverse slip near the surface to normal slip at a depth of 3–4 km. However, the downward motion of the caldera block caused by the normal-slipping ring fault is inconsistent with the upward motion due to the opening crack. Therefore, we consider this trapdoor faulting motion is unrealistic. In contrast, when we assume that the horizontal crack is at a depth of 3 km (Figure 3b), the ring fault motion becomes reverse slip at all depths and consistent with the opening crack motion Thus, we adopt models with a relatively shallow horizontal crack at a depth of 3 km. In Figure 4b, we show the tsunami waveform misfits of the shallower source models are similarly small, irrespective of the dip angle and arc length of the ring fault. This indicates that the tsunami data provide little constraint on the ring fault parameters.

In contrast, the long-period seismic data are useful for obtaining a best-fit source model with constraints on the dip angle and arc length of the ring fault. The amplitudes of the long-period seismic waves from the models depend strongly on the assumed ring fault dip angle, whereas similar moment magnitudes and slip amounts of the models are obtained by the tsunami waveform inversion (Figure S6). This is because the ring faulting becomes more inefficient in radiating seismic waves as the dip angle becomes closer to the vertical (Sandanbata, Kanamori, et al., 2021). Additionally, in our previous study (Sandanbata, Kanamori, et al., 2021), we showed that the seismic radiation pattern from ring faulting is sensitive to the arc length. Because of these seismic characters of the ring fault, the seismic waveform misfit changes largely depending of the two assumed ring fault parameters of the models (Figure 4b), which helps us find a source model with the best combination of the ring fault dip angle and arc length that minimizes the seismic waveform misfit (85.0° and a two-third ring, respectively). A previous study (Kodaira et al., 2007) detected a very low-velocity layer in the shallowest crust along the Izu–Bonin arc. If we assume a lower velocity in the shallowest crust, then our estimate of the ring fault dip angle decreases to ~77° (Text S2; Figure S7).

Figure 3b shows our best-fit source model for the 2015 earthquake. In summary, the model has an inward-dipping ring fault with a dip angle of 85° along two-thirds of the ring arc length of the caldera rim, and a horizontal crack at a depth of 3 km. The ring fault has a maximum reverse slip of 5.6 m on its northeastern side. The vertical opening of the horizontal crack is a maximum of 3.0 m on its eastern side, whereas its closure is 5.3 m on its southwestern side. The model causes asymmetric motion of the caldera block, with a maximum upward displacement of 3.4 m along the northeastern part of the ring fault and a maximum downward displacement of 1.3 m along the southwestern part of the crack (Figure 3c). The resultant net volume increase of the horizontal crack is 1.11×10^7 m^3. The vertical sea-surface displacement caused by the model (Figure 5a) contains twice larger and more localized uplift, compared to our preliminary analysis result (Figure 2a), but can well explain the tsunami waveform data at all the OBP gauges (Figure 5b). Note that in the preliminary analysis, the main uplift was estimated in a relatively broader area (Figure 2a) because of no constraint from the source structure, which possibly led to underestimation of the amplitude. The moment tensor of the source model (Figure

6a) has a large isotropic component and can be decomposed into a horizontal crack and ring fault (Figure 6b). This model well explains the long-period seismic data at most stations (Figure 6c). The waveform discrepancy at a few stations (e.g., KZS and YMZ) can be reduced by slightly modifying the dip angles of parts of the ring fault (Text S3; Figure S8).

6 Discussion

6.1 Submarine trapdoor faulting at Sumisu caldera

Our source model (Figure 3b) suggests that submarine trapdoor faulting at Sumisu caldera, driven by overpressure of magma accumulating in the horizontal crack or a sill-like reservoir, caused the 2015 earthquake and tsunami (Figure 3a). We suggest that continuous magma supply into the crack increases the shear stress on the pre-existing ring fault system until it reaches a critical value for initiation of brittle rupture of the ring fault. Once the trapdoor faulting process initiates with the ring faulting, the top surface of the horizontal crack moves vertically upward. The consequent increase of the reservoir volume depressurizes the inner magma, possibly causing the closure of the southwestern part of the crack. Due to the volume increase and depressurization of the reservoir, the trapdoor faulting may not lead to an immediate submarine eruption at the caldera (Amelung et al., 2000).

The proposed source model shares many similarities with the model and observations at the Sierra Negra caldera. At this subaerial caldera in the Galápagos Islands, several trapdoor faulting events occurred with vertical-T CLVD earthquakes of $M_w \sim 5$ due to a pressurized sill-like magma reservoir located at ~2 km depth (Amelung et al., 2000; Jónsson, 2009). These events caused meter-scale uplift on the southern part of the caldera floor. For example, a Global

Positioning System sensor near the intra-caldera fault recorded an upward displacement of 84 cm within 10 s of the time of trapdoor faulting in 2005 (Chadwick et al., 2006; Jónsson, 2009). The duration of the deformation was comparable to the rupture duration (10 s) of the 2015 earthquake at Sumisu caldera, as estimated by our moment tensor analysis (Text S1; Table S3). In addition, during the 2005 trapdoor faulting at Sierra Negra, the northern caldera floor subsided by a few centimeters, which was attributed to the pressure drop of the inner magma reservoir due to the trapdoor faulting (Jónsson, 2009; Zheng et al., 2021). This observation is similar to that expected from our model with closure of a crack in the southwestern part of Sumisu caldera. Our discovery of submarine trapdoor faulting, following previous observations at the subaerial Sierra Negra caldera, indicates that this volcanic process might be more common at calderas than previously thought.

6.2 Efficient tsunami generation mechanism

Trapdoor faulting produces an unusually large slip as compared with ordinary tectonic earthquakes, and can generate a large tsunami despite its moderate-sized earthquake magnitude when it occurs under water. For the 2015 earthquake (M_w 5.7), our best-fit source model has a maximum slip of 5.6 m along the ring fault (Figure 3b). In contrast, the empirical scaling law (Wells & Coppersmith, 1994) predicts that tectonic earthquakes with the same moment magnitude have a maximum slip of only 0.17 m. The subaerial trapdoor faulting in 2005 at the Sierra Negra caldera also caused a large slip of ~2 m along the intra-caldera fault, despite its small seismic body-wave magnitude of 4.6 (Jónsson, 2009; Zheng et al., 2021). Such disproportionately large slips due to trapdoor faulting possibly reflect the shallow source depth, localized stress increase due to magma overpressure, and/or fault–reservoir interaction during rupture.

Submarine trapdoor faulting is even more efficient in generating tsunamis, given the relatively low seismic magnitude of the earthquakes, due to its shallow and complex source structure. Firstly, trapdoor faulting occurring above a shallow magma reservoir at a depth of <3 km is more tsunamigenic, because it more efficiently deforms seafloor than tectonic earthquakes that typically occur at a depth of >10 km (Ward, 1982). Secondly, the combination of reverse slip along the ring fault and vertical motion of the horizontal crack localizes the coseismic uplift on a small area within the circular ring fault (Figure 5a). As such, trapdoor faulting can generate larger tsunamis than ordinary seismic faults of an equivalent fault size. However, at such shallow depths, the vertical motion of the horizontal crack and two moment tensor elements, $M_{r\theta}$ and $M_{r\phi}$, of the ring fault are inefficient in radiating long-period seismic waves (Fukao et al., 2018; Sandanbata, Kanamori, et al., 2021), which reduces the seismic magnitude.

To examine the inefficient generation of seismic waves, Figure 7 shows long-period seismograms computed from the three moment tensors from our source model (Figure S8): (a) the total moment tensor combining the ring fault and horizontal crack ($\boldsymbol{M_{HC}} + \boldsymbol{M_{RF}}$); (b) the ring fault only ($\boldsymbol{M_{RF}}$); and (c) the ring fault only, but without $M_{r\theta}$ and $M_{r\phi}$ (i.e., M_{rr}, $M_{\theta\theta}$, $M_{\phi\phi}$, and $M_{\theta\phi}$ of $\boldsymbol{M_{RF}}$). Although the seismic magnitudes and focal mechanisms of the three moment tensors are different, their synthetic seismograms are similar. This highlights the very small contributions from the horizontal crack and two moment tensor elements ($M_{r\theta}$ and $M_{r\phi}$) of the ring fault. Despite the seismic magnitude M_w 6.15 of $\boldsymbol{M_{HC}} + \boldsymbol{M_{RF}}$ (a seismic moment $M_0 = 2.13 \times 10^{18}$ Nm; Figure 7a), only part of the ring faulting with M_w 5.72 ($M_0 = 4.74 \times 10^{17}$ Nm; equivalent to 22% of the total seismic moment; Figure 7c) contributes to the long-period seismic radiation of the trapdoor faulting. We note that the four moment tensor elements of the ring fault contributing to the seismic waves constitute a vertical-T CLVD-type moment tensor, which agrees with the solution reported in the GCMT catalogue (Ekström et al., 2012) (Figure 1b).

6.3 Quasi-regular recurrence of submarine trapdoor faulting

We suggest that continuous magma supply below Sumisu caldera causes submarine trapdoor faulting almost every decade. By additional moment tensor analysis using long-period seismic data (Text S3), we estimate the resolvable moment tensors $\boldsymbol{M_{res}}$ of the four earthquakes, which were proposed in our previous study (Sandanbata, Kanamori, et al., 2021) for constraining the ring fault geometry. The resolvable moment tensors characterized by the null-axis direction and ratio of the vertical-CLVD component (k_{CLVD}) are similar for the 1996, 2006, and 2015 earthquakes (Figure 8a). These similarities indicate that, at the times of the earthquakes, trapdoor faulting occurred along almost the same ring fault segment of the source model for the 2015 earthquake (Figure 3b). This interpretation is supported by their similar tsunami waveforms recorded at tide gauges (Figures 1d–e and S1). The overall recurrence interval of ~10 yr may correspond to the time required to accumulate enough magma overpressure within the reservoir to rupture the ring fault (Cabaniss et al., 2020; Gregg et al., 2018). On the other hand, the resolvable moment tensor for the 2018 earthquake, which occurred only three years after the 2015 earthquake, contains a more dominant double-couple component (i.e., smaller k_{CLVD}) and has a smaller moment magnitude M_w (Figure 8a), suggesting that the trapdoor faulting in 2018 caused a rupture along a ring fault segment with a shorter arc length than for the other events. This may explain the smaller tsunami associated with the 2018 earthquake (Figures 1d–e and S1). Some complexities linked to source geometries, frictional properties along the ring fault, or magma supply rate may cause variations in the size, ring fault length, and recurrence interval of trapdoor faulting.

The topography of Sumisu caldera also reflects the longer term recurrence of trapdoor faulting. Our source model predicts that the submarine trapdoor faulting in 2015 uplifted the northeastern part of the caldera floor, but led to little deformation in its southwestern part (Figure 8b). Along a SW–NE profile across the caldera, coseismic vertical displacement with an offset of about 4 m (A–A') correlates with the caldera floor topography, which slopes upward from the SW to NE with an altitude offset of ~150 m (B–B') (Figure 8c). A similar correlation was found at the Sierra Negra caldera (Amelung et al., 2000), where trapdoor faulting has occurred repeatedly due to continuous magma input. This suggests that magma supply has been continuous at Sumisu caldera, thereby causing repeated submarine trapdoor faulting and forming the sloping floor inside the caldera. Since an explosive submarine eruption in 1916 (Japan Meteorological Agency, 2013), no clear evidence of eruptions has been found at Sumisu caldera and the relationship between trapdoor faulting and eruptions is still unclear.

6.4 Mechanisms of volcanic tsunami generation

Various mechanisms have been proposed to generate volcanic tsunamis: submarine explosions, pyroclastic flows, flank failures, caldera collapses, volcanic earthquakes accompanying eruptions, and shock waves due to explosions (Paris, 2015; Paris et al., 2014). The submarine trapdoor faulting mechanism identified in this study may be categorized as a volcanic earthquake mechanism, but is characterized by large-amplitude tsunamis without significant seismic radiation and a quasi-regular recurrence. This mechanism may also explain unusual tsunamis with similar characteristics generated near the volcanic islands in the Kermadec Arc, north of New Zealand (Gusman et al., 2020). These volcanic tsunamis due to submarine trapdoor faulting suggest that continuous monitoring of submarine calderas is necessary to robustly assess tsunami hazards.

7 Conclusions

By using remotely observed tsunami and long-period seismic data for the 2015 earthquake at Sumisu caldera, we constructed a source model of submarine trapdoor faulting, which can quantitatively explain both datasets. The combined waveform analyses also allow us to constrain the magma reservoir depth and ring fault geometry. Based on the model, we show that the atypical source properties, or large slip on a shallow and complex structure, contributed to meter-scale tsunami generation despite the moderate seismic magnitude. The sub-decadal recurrence of trapdoor faulting with similar tsunamis and seismic characteristics suggests continuous magma supply into the submarine caldera is taking place. Further investigations of the submarine caldera using *in situ* geophysical instruments, such as hydrophones, seismometers, or pressure sensors, and ship-borne surveys will be useful for understanding the volcanism, including the magma accumulation process. This may lead to improved predictions of future submarine trapdoor faulting and/or eruptions.

Acknowledgments

We thank Aditya Gusman for providing the digitized tide gauge data. We thank Yoshio Fukao, Hiroko Sugioka, Aki Ito, and Hajime Shiobara for helping obtain some of the tsunami data. This research was funded by JSPS KAKENHI (Grants JP17J02919, JP20J01689, and JP19K04034) and JST J-RAPID (Grant JPMJJR1805). The travel of Osamu Sandanbata to the California Institute of Technology was supported by the Overseas Internship Program of the Earthquake Research Institute, The University of Tokyo.

Open Research

The earthquake data are from the Global CMT catalogue (https://www.globalcmt.org/). Tide gauge data are available on request from the Japan Meteorological Agency (https://www.jma.go.jp/jma/indexe.html) and Hydrographic and Oceanographic Department, Japan Coast Guard (https://www1.kaiho.mlit.go.jp/jhd-E.html). Bathymetric data are available from the Japan Hydrographic Association (https://www.jha.or.jp/en/jha/) and GEBCO Compilation Group (https://www.gebco.net/). OBP data are available from the Japan Agency for Marine-Earth Science and Technology (http://p21.jamstec.go.jp/top/), National Research Institute for Earth Science and Disaster Resilience (https://www.seafloor.bosai.go.jp/), and National Oceanic and Atmospheric Administration (https://nctr.pmel.noaa.gov/Dart/). Seismic data are available from the NIED (https://www.fnet.bosai.go.jp/top.php) and Incorporated Research Institutions for Seismology (https://ds.iris.edu/wilber3/find_event). The source models presented in this paper are detailed in Data Set S1.

References

Aki, K., & Richards, P. G. (1980). *Quantitative seismology: theory and methods* (Vol. 842). Freeman San Francisco, CA.

Amelung, F., Jónsson, S., Zebker, H., & Segall, P. (2000). Widespread uplift and 'trapdoor' faulting on Galápagos volcanoes observed with radar interferometry. *Nature*, *407*(6807), 993–996.

Baba, T., Takahashi, N., Kaneda, Y., Ando, K., Matsuoka, D., & Kato, T. (2015). Parallel Implementation of Dispersive Tsunami Wave Modeling with a Nesting Algorithm for the 2011 Tohoku Tsunami. *Pure and Applied Geophysics*, *172*(12), 3455–3472.

Cabaniss, H. E., Gregg, P. M., Nooner, S. L., & Chadwick, W. W., Jr. (2020). Triggering of eruptions at Axial Seamount, Juan de Fuca Ridge. *Scientific Reports*, *10*(1), 10219.

Chadwick, W. W., Geist, D. J., Jónsson, S., Poland, M., Johnson, D. J., & Meertens, C. M. (2006). A volcano bursting at the seams: Inflation, faulting, and eruption at Sierra Negra volcano, Galápagos. *Geology*, *34*(12), 1025–1028.

Chikasada, N. Y. (2019). Short-wavelength Tsunami Observation Using Deep Ocean Bottom Pressure Gauges. In *The 29th International Ocean and Polar Engineering Conference*. International Society of Offshore and Polar Engineers. Retrieved from https://onepetro.org/conference-paper/ISOPE-I-19-707

Cole, J. W., Milner, D. M., & Spinks, K. D. (2005). Calderas and caldera structures: a review. *Earth-Science Reviews*, *69*(1), 1–26.

Dahlen, F. A., & Tromp, J. (1998). *Theoretical Global Seismology*. Princeton University Press.

Duputel, Z., Rivera, L., Kanamori, H., & Hayes, G. (2012). W phase source inversion for moderate to large earthquakes (1990–2010). *Geophysical Journal International*, *189*(2), 1125–1147.

Ekström, G. (1994). Anomalous earthquakes on volcano ring-fault structures. *Earth and Planetary Science Letters*, *128*(3–4), 707–712.

Ekström, G., Nettles, M., & Dziewoński, A. M. (2012). The global CMT project 2004–2010: Centroid-moment tensors for 13,017 earthquakes. *Physics of the Earth and Planetary Interiors*, *200–201*, 1–9.

Fukao, Y., Sandanbata, O., Sugioka, H., Ito, A., Shiobara, H., Watada, S., & Satake, K. (2018). Mechanism of the 2015 volcanic tsunami earthquake near Torishima, Japan. *Science Advances*, *4*(4), eaao0219.

Gregg, P. M., Le Mével, H., Zhan, Y., Dufek, J., Geist, D., & Chadwick, W. W., Jr. (2018). Stress triggering of the 2005 eruption of Sierra Negra volcano, Galápagos. *Geophysical Research Letters*, *45*(24), 13288–13297.

Grilli, S. T., Tappin, D. R., Carey, S., Watt, S. F. L., Ward, S. N., Grilli, A. R., et al. (2019). Modelling of the tsunami from the December 22, 2018 lateral collapse of Anak Krakatau volcano in the Sunda Straits, Indonesia. *Scientific Reports*, *9*(1), 11946.

Gusman, A. R., Kaneko, Y., Power, W., & Burbidge, D. (2020). Source process for two enigmatic repeating vertical‐T CLVD tsunami earthquakes in the kermadec ridge. *Geophysical Research Letters*, *47*(16). https://doi.org/10.1029/2020gl087805

Hanks, T. C., & Kanamori, H. (1979). A moment magnitude scale. *Journal of Geophysical Research*, *84*(B5), 2348.

Hayes, G. P., Rivera, L., & Kanamori, H. (2009). Source Inversion of the W-Phase: Real-time Implementation and Extension to Low Magnitudes. *Seismological Research Letters*, *80*(5), 817–822.

Herrmann, R. B. (2013). Computer programs in seismology: An evolving tool for instruction and research. *Seismological Research Letters*, *84*(6), 1081–1088.

Ho, T.-C., Satake, K., & Watada, S. (2017). Improved phase corrections for transoceanic tsunami data in spatial and temporal source estimation: Application to the 2011 Tohoku earthquake. *Journal of Geophysical Research, [Solid Earth]*, *122*(12), 10155–10175.

Hossen, M. J., Cummins, P. R., Dettmer, J., & Baba, T. (2015). Time reverse imaging for far-field tsunami forecasting: 2011 Tohoku earthquake case study. *Geophysical Research Letters*, *42*(22), 9906–9915.

Hunt, J. E., Tappin, D. R., Watt, S. F. L., Susilohadi, S., Novellino, A., Ebmeier, S. K., et al. (2021). Submarine landslide megablocks show half of Anak Krakatau island failed on December 22nd, 2018. *Nature Communications*, *12*(1), 2827.

Japan Meteorological Agency. (2013). NATIONAL CATALOGUE OF THE ACTIVE VOLCANOES IN JAPAN. Retrieved from https://www.data.jma.go.jp/svd/vois/data/tokyo/STOCK/souran_eng/menu.htm

Jónsson, S. (2009). Stress interaction between magma accumulation and trapdoor faulting on Sierra Negra volcano, Galápagos. *Tectonophysics*, *471*(1), 36–44.

Kajiura, K. (1963). The Leading Wave of a Tsunami. *Bulletin of the Earthquake Research Institute, University of Tokyo*, *41*(3), 535–571.

Kanamori, H. (1972). Mechanism of tsunami earthquakes. *Physics of the Earth and Planetary Interiors*, *6*(5), 346–359.

Kanamori, H. (1977). The energy release in great earthquakes. *Journal of Geophysical Research*, *82*(20), 2981–2987.

Kanamori, H., & Rivera, L. (2008). Source inversion of Wphase: speeding up seismic tsunami warning. *Geophysical Journal International*, *175*(1), 222–238.

Kanamori, H., Ekström, G., Dziewonski, A., Barker, J. S., & Sipkin, S. A. (1993). Seismic radiation by magma injection: An anomalous seismic event near Tori Shima, Japan. *Journal of Geophysical Research*, *98*(B4), 6511–6522.

Kawakatsu, H., & Yamamoto, M. (2015). Volcano Seismology. In G. Schubert (Ed.), *Treatise on Geophysics (Second Edition)* (pp. 389–419). Oxford: Elsevier.

Kodaira, S., Sato, T., Takahashi, N., Ito, A., Tamura, Y., Tatsumi, Y., & Kaneda, Y. (2007). Seismological evidence for variable growth of crust along the Izu intraoceanic arc. *Journal of Geophysical Research*, *112*(B5). https://doi.org/10.1029/2006jb004593

Nikkhoo, M., & Walter, T. R. (2015). Triangular dislocation: an analytical, artefact-free solution. *Geophysical Journal International*, *201*(2), 1119–1141.

Paris, R. (2015). Source mechanisms of volcanic tsunamis. *Philosophical Transactions. Series A, Mathematical, Physical, and Engineering Sciences*, *373*(2053). https://doi.org/10.1098/rsta.2014.0380

Paris, R., Switzer, A. D., Belousova, M., Belousov, A., Ontowirjo, B., Whelley, P. L., & Ulvrova, M. (2014). Volcanic tsunami: a review of source mechanisms, past events and hazards in Southeast Asia (Indonesia, Philippines, Papua New Guinea). *Natural Hazards*, *70*(1), 447–470.

Peregrine, D. H. (1972). Equations for Water Waves and the Approximation behind Them. In R. E. Meyer (Ed.), *Waves on Beaches and Resulting Sediment Transport* (pp. 95–121). Academic Press.

Persson, P.-O., & Strang, G. (2004). A Simple Mesh Generator in MATLAB. *SIAM Review. Society for Industrial and Applied Mathematics*, *46*(2), 329–345.

Sandanbata, O., Kanamori, H., Rivera, L., Zhan, Z., Watada, S., & Satake, K. (2021). Moment tensors of ring-faulting at active volcanoes: Insights into vertical-CLVD earthquakes at the Sierra Negra caldera, Galápagos islands. *Journal of Geophysical Research, [Solid Earth]*, *126*(6), e2021JB021693.

Sandanbata, O., Watada, S., Ho, T.-C., & Satake, K. (2021). Phase delay of short-period tsunamis in the density-stratified compressible ocean over the elastic Earth. *Geophysical Journal International*, *226*(3), 1975–1985.

Satake, K. (2015). 4.19 - Tsunamis. In G. Schubert (Ed.), *Treatise on Geophysics (Second Edition)* (pp. 477–504). Oxford: Elsevier.

Satake, K., & Kanamori, H. (1991). Abnormal tsunamis caused by the June 13, 1984, Torishima, Japan, earthquake. *Journal of Geophysical Research*, *96*(B12), 19933–19939.

Shukuno, H., Tamura, Y., Tani, K., Chang, Q., Suzuki, T., & Fiske, R. S. (2006). Origin of silicic magmas and the compositional gap at Sumisu submarine caldera, Izu–Bonin arc, Japan. *Journal of Volcanology and Geothermal Research*, *156*(3), 187–216.

Shuler, A., Nettles, M., & Ekström, G. (2013). Global observation of vertical-CLVD earthquakes at active volcanoes. *Journal of Geophysical Research, [Solid Earth]*, *118*(1), 138–164.

Shuler, A., Ekström, G., & Nettles, M. (2013). Physical mechanisms for vertical-CLVD earthquakes at active volcanoes. *Journal of Geophysical Research, [Solid Earth]*, *118*(4), 1569–1586.

Silver, P. G., & Jordan, T. H. (1982). Optimal estimation of scalar seismic moment. *Geophysical Journal International*, *70*(3), 755–787.

Tani, K., Fiske, R. S., Tamura, Y., Kido, Y., Naka, J., Shukuno, H., & Takeuchi, R. (2008). Sumisu volcano, Izu-Bonin arc, Japan: site of a silicic caldera-forming eruption from a small open-ocean island. *Bulletin of Volcanology*, *70*(5), 547–562.

Tappin, D. R., Matsumoto, T., Watts, P., Satake, K., McMurtry, G. M., Matsuyama, M., et al. (1999). Sediment slump likely caused 1998 Papua New Guinea tsunami. *Eos*, *80*(30), 329.

Walter, T. R., Haghshenas Haghighi, M., Schneider, F. M., Coppola, D., Motagh, M., Saul, J., et al. (2019). Complex hazard cascade culminating in the Anak Krakatau sector collapse. *Nature Communications*, *10*(1), 4339.

Ward, S. N. (1982). On tsunami nucleation II. An instantaneous modulated line source. *Physics of the Earth and Planetary Interiors*, *27*, 273–285.

Ward, S. N. (2001). Landslide tsunami. *Journal of Geophysical Research*, *106*(B6), 11201–11215.

Wells, D. L., & Coppersmith, K. J. (1994). New Empirical Relationships among Magnitude, Rupture Length, Rupture Width, Rupture Area, and Surface Displacement. *Bulletin of the Seismological Society of America*, *84*(4), 974–1002.

Yun, S.-H. (2007). *A mechanical model of the large-deformation 2005 Sierra Negra volcanic eruption derived from InSAR measurements*. stanford.edu. Retrieved from https://web.stanford.edu/group/radar/people/Yun_thesis_small.pdf

Zheng, Y., Blackstone, L. A., & Segall, P. (2021, October 15). *Constraints on absolute chamber volume from geodetic measurements: Trapdoor faulting in the Galapagos*. https://doi.org/10.1002/essoar.10508257.1

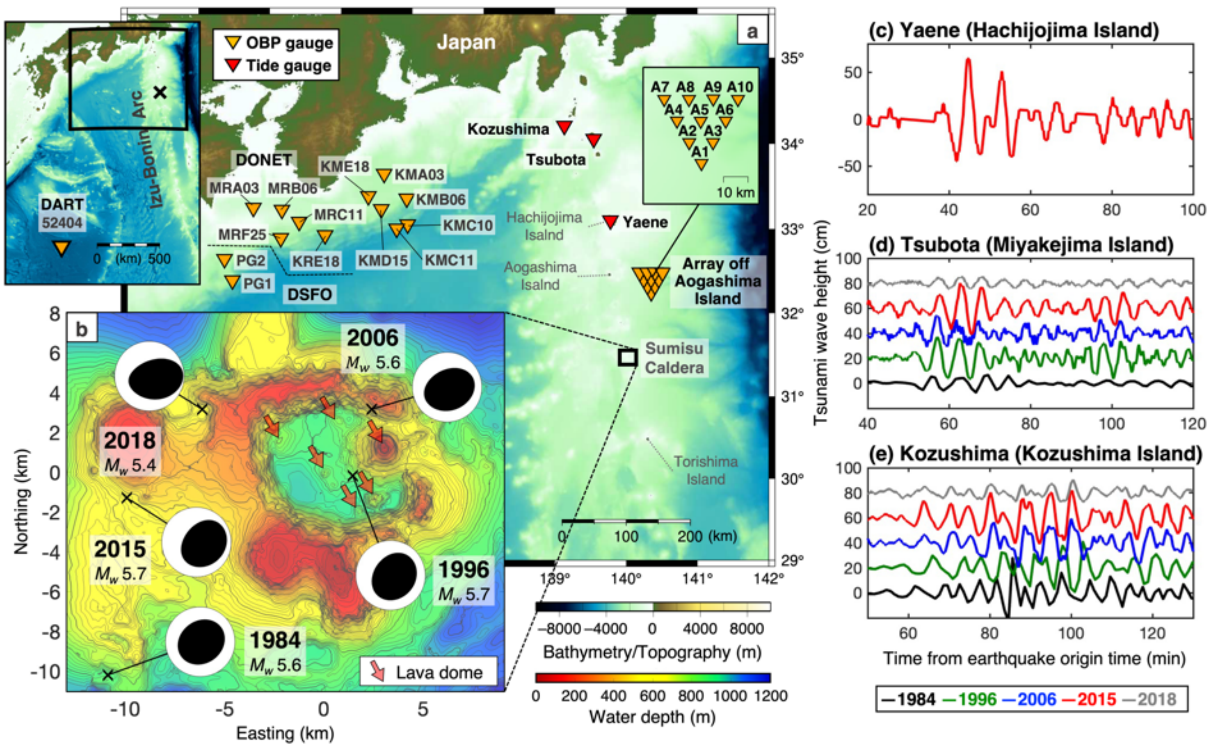

Figure 1. Anomalous tsunamis due to volcanic earthquakes at Sumisu caldera. (**a**) Map showing the locations of Sumisu caldera, ocean bottom pressure gauges (orange triangles), and representative tide gauges (red triangles). (**b**) Repeating earthquakes near Sumisu caldera reported by the Global CMT (GCMT) catalog (Ekström et al., 2012). The focal mechanisms are shown by projection onto the lower focal hemisphere. Arrows indicate lava domes on the caldera floor (Tani et al., 2008). (**c**) Tsunami waveform from the 2015 earthquake recorded by the tide gauge at Yaene (Hachijojima Island). (**d**–**e**) Tsunami waveforms at Tsubota (Miyakejima Island) and Kozushima (Kozushima Island) from the repeating earthquakes. Baselines for different events are shifted by multiples of 20 cm. Tsunami waveforms at other tide gauge stations are shown in Figure S1.

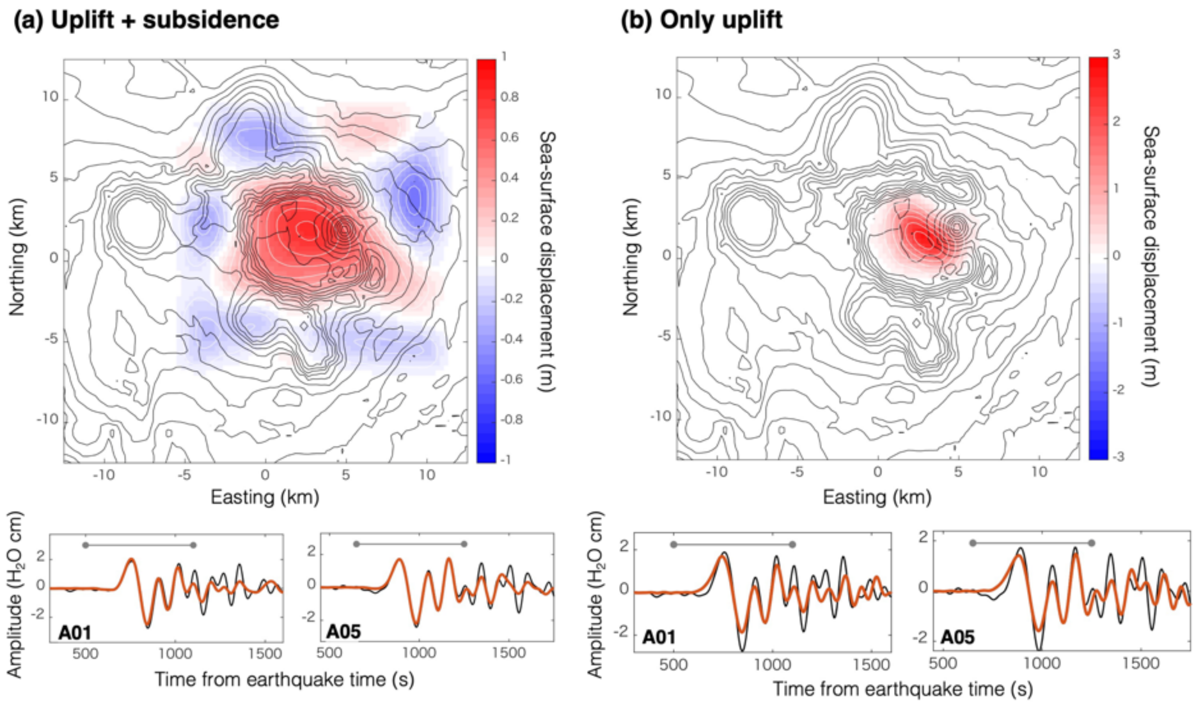

Figure 2. Preliminary initial sea-surface displacement models. Models with (**a**) both uplift and subsidence and (**b**) only uplift. (Top panel) Bathymetric contours at 100 m intervals. (Bottom panels) Comparison of the observed (black) and synthetic (red) tsunami waveforms at representative ocean bottom pressure gauges. The gray line represents the time interval used for the inversion.

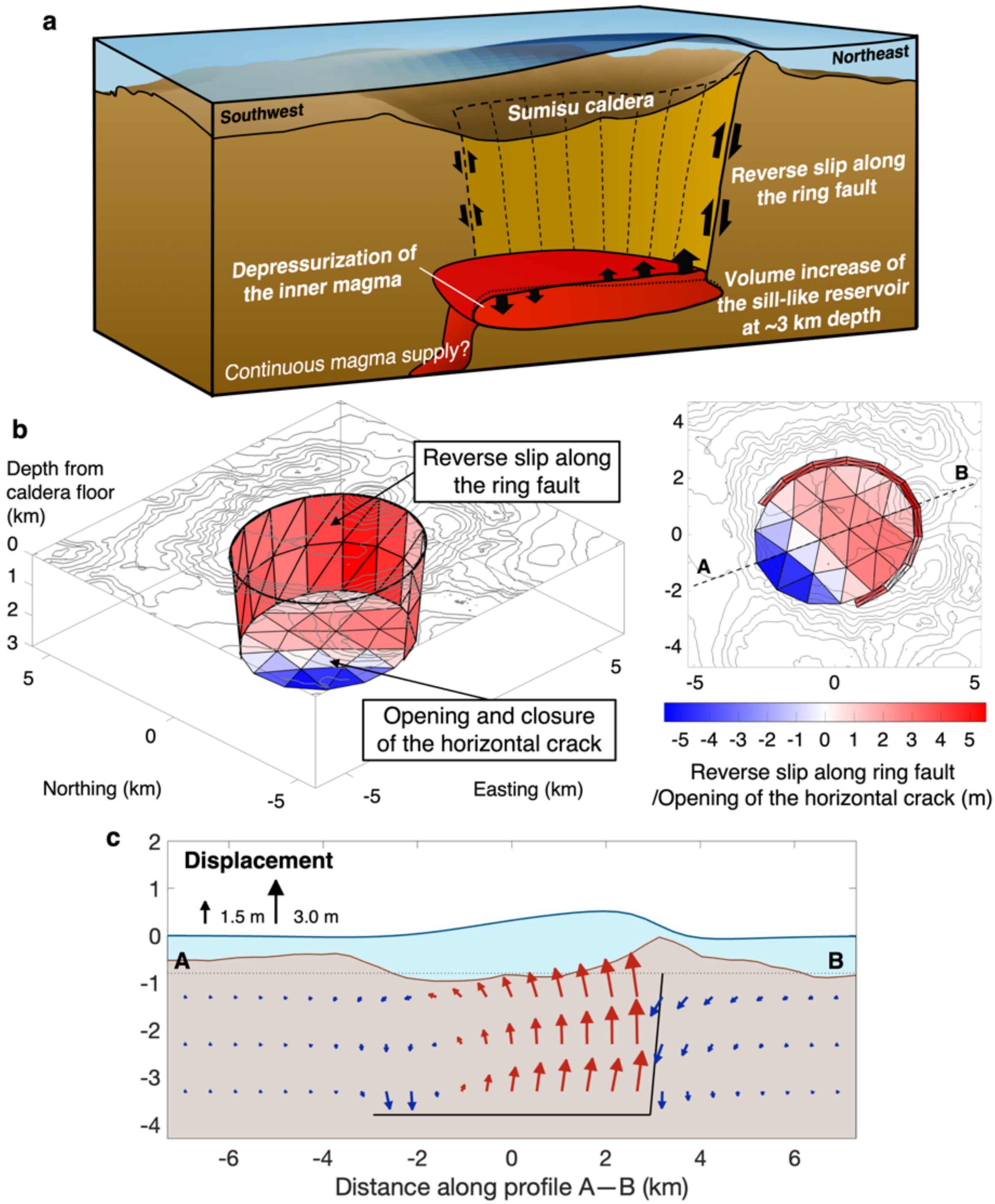

Figure 3. Submarine trapdoor faulting mechanism at Sumisu caldera. (**a**) Schematic illustration of the mechanism (not to scale). Reverse slip occurs along the ring fault, the sill-like reservoir inflates on the northeastern side of the caldera, and consequent depressurization of the inner

magma causes the downward motion of the upper wall of the southwestern part of the magma reservoir. (**b**) Best-fit source model for the 2015 earthquake viewed from southwest (left panel) and above (right panel). The horizontal crack is at a depth of 3 km, and the ring fault along two-thirds of the arc of the caldera rim has a uniform dip angle of 85°. The red color on the ring fault represents reverse slip. Red and blue colors on the horizontal crack represent vertical opening and closure, respectively. (**c**) Displacement of the caldera computed with the model along the A–B profile shown in (**b**) (right panel). We assume the bathymetry is flat for the computation. Note that the seafloor and sea-surface displacements are exaggerated.

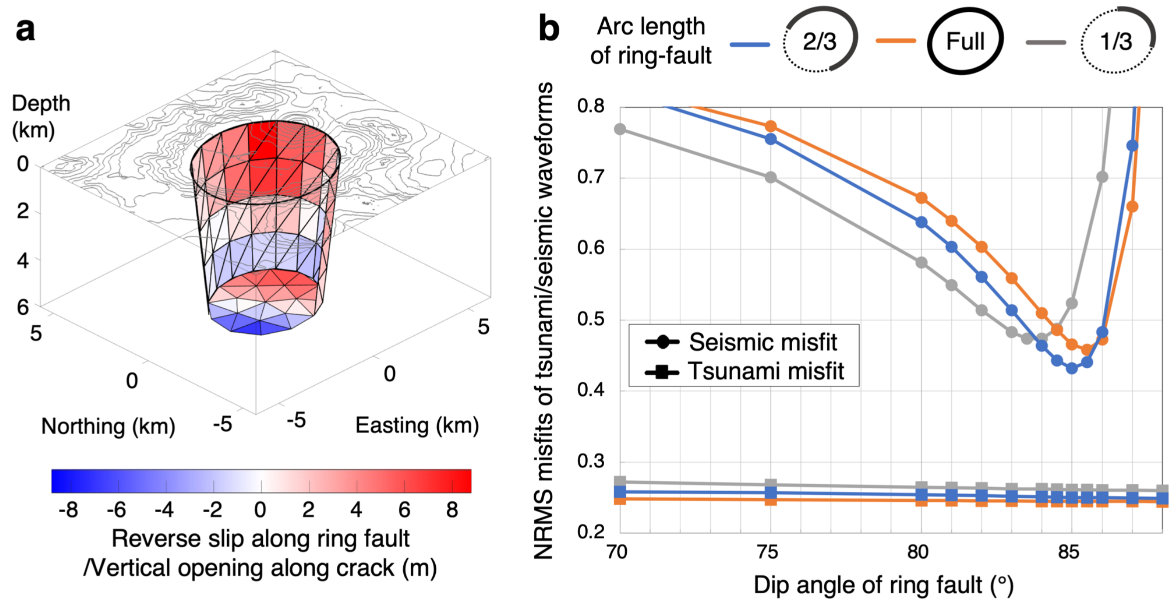

Figure 4. Constraints on the geometrical source parameters from the tsunami and seismic analysis. (**a**) Source model inverted from the tsunami waveform inversion, in which we assume a horizontal crack at a depth of 6 km. Color coding is the same as for Figure 3b, but the blue color on the ring fault indicates normal slip. We consider this model to be unrealistic (see the text for explanation). (**b**) Comparison of the tsunami and seismic waveform misfits (Equations 7 and 10, respectively) for source models with different ring fault dip angles and arc lengths. All the models shown in (**b**) have the horizontal crack at a depth of 3 km.

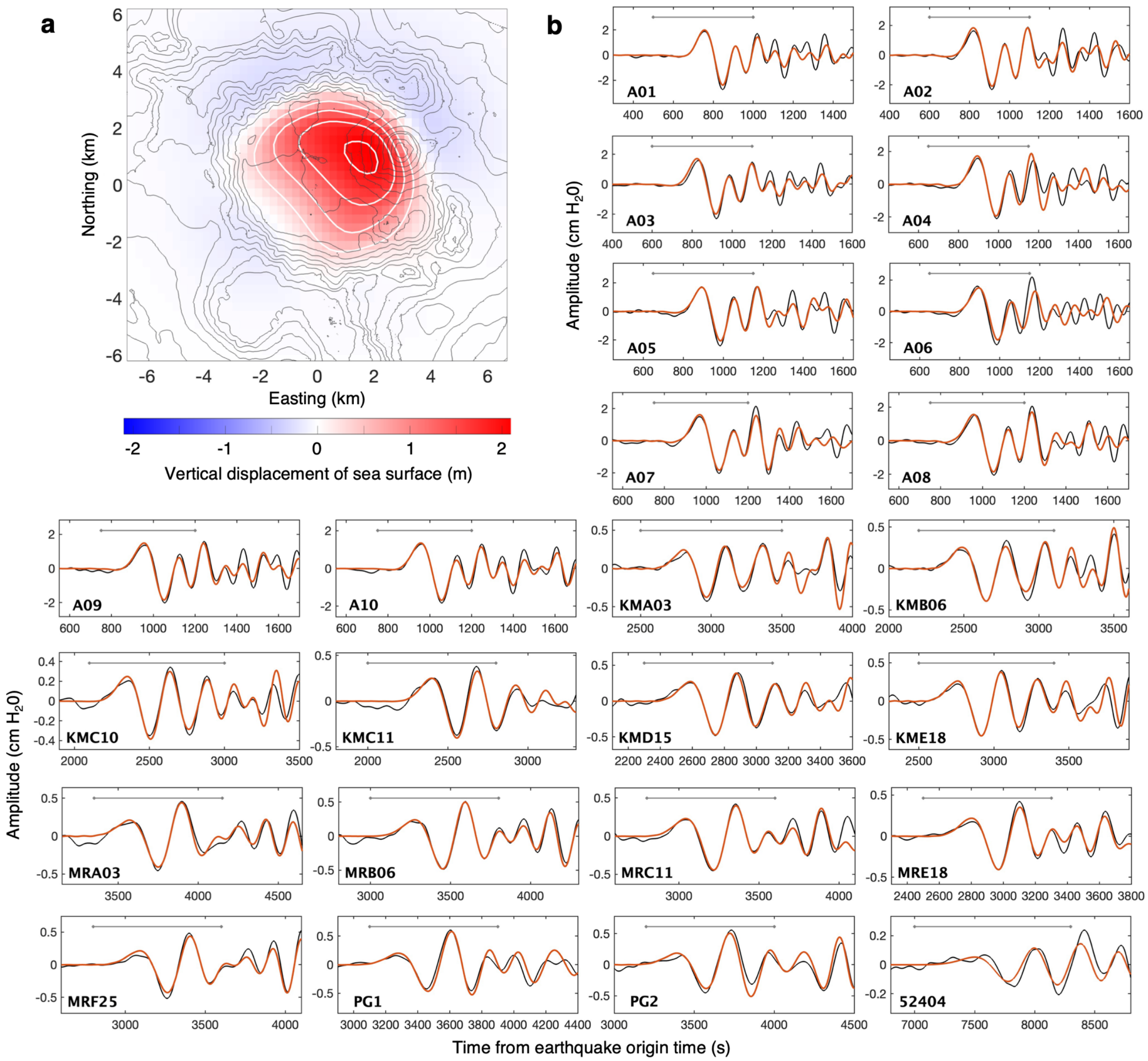

Figure 5. Tsunami waveforms from the best-fit source model (Figure 3b). (**a**) Vertical sea-surface displacement. Red and blue colors represent uplift and subsidence, respectively, with white contour lines plotted every 0.5 m. (**b**) Comparison of the observed (black) and synthetic (red) tsunami waveforms from the model at the ocean bottom pressure gauges. The gray line represents the time interval used for the inversion.

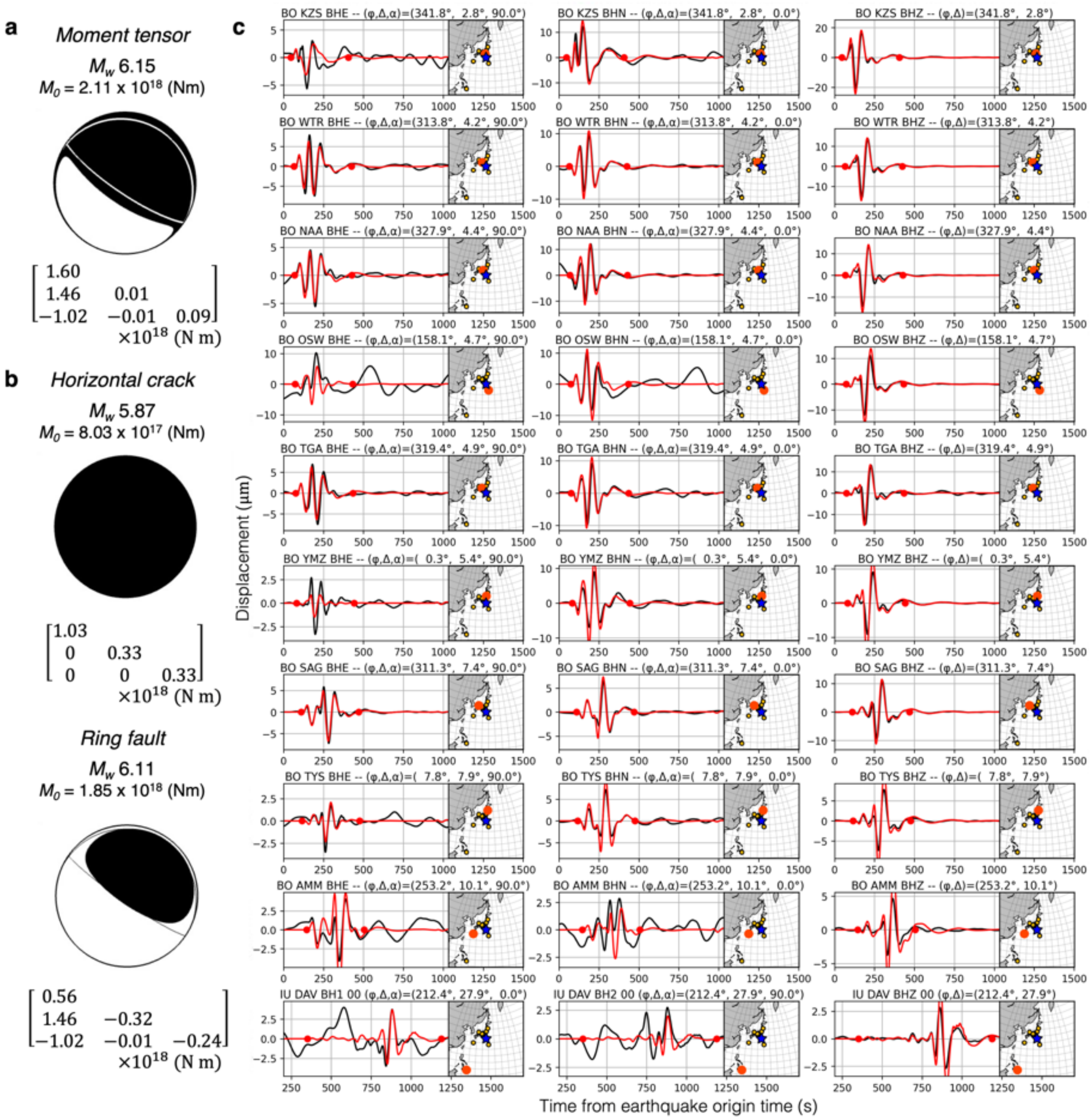

Figure 6. Long-period seismograms from the best-fit source model (Figure 3b). (**a**) Moment tensors of the model and (**b**) horizontal crack and ring fault. The focal mechanisms are shown as projections onto the lower focal hemisphere, and the orientation of the best double-couple solution is shown as thin lines. (**c**) Comparison of the observed (black) and synthetic (red) seismograms (period = 60–250 s), computed with the moment tensor shown in (**a**) at representative stations. The data interval used to calculate the waveform misfit is delimited by

the red dots. In each inset figure, a large red circle and blue star represent the station and earthquake centroid, respectively. The record component, station azimuth (φ), and epicentral distance (Δ) are given on the top of each panel, and the azimuth of each component measured clockwise from north (α) is given for the horizontal components.

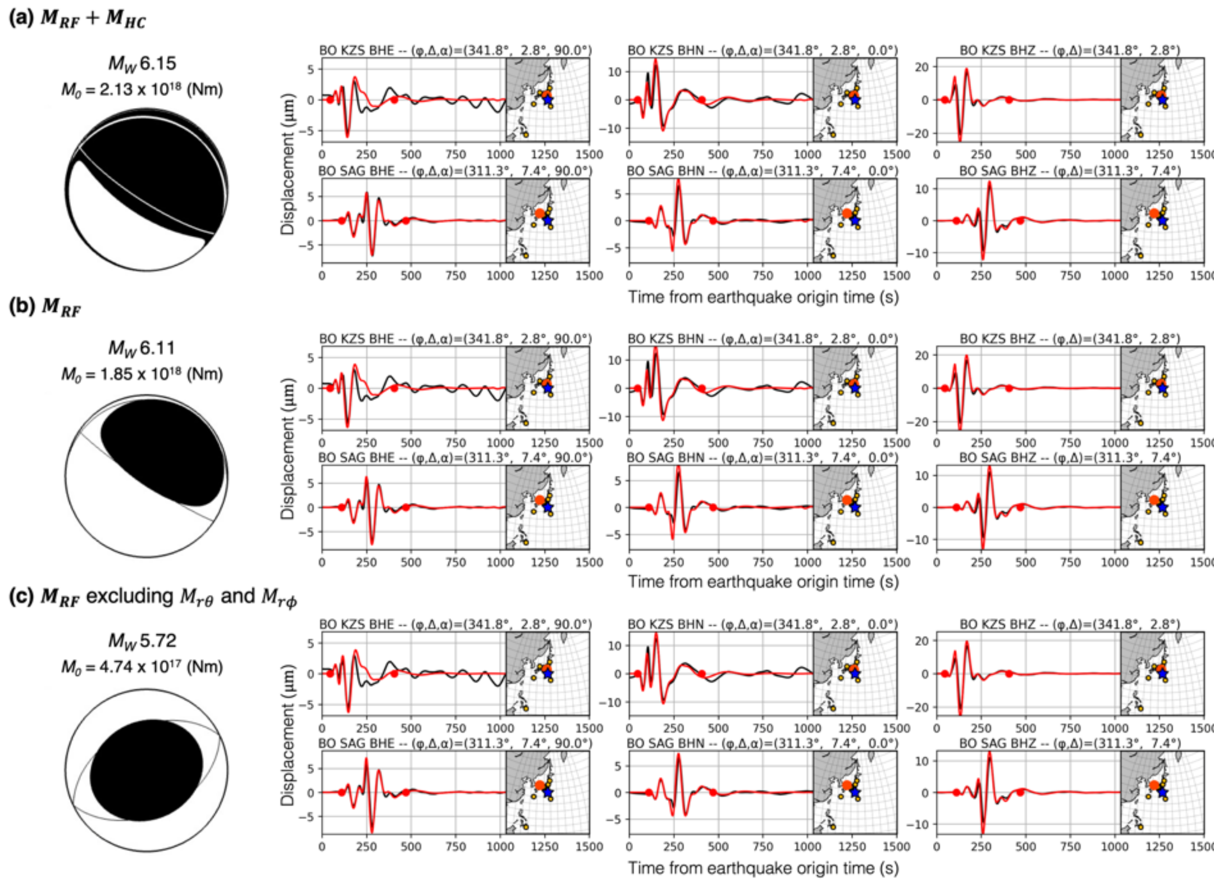

Figure 7. Contributions to the long-period seismic waves of the source model with the modified ring fault dip angles (Figure S8). Synthetic seismograms (red curves) from the moment tensors of (**a**) a combination of the ring fault and horizontal crack, $\boldsymbol{M_{RF}} + \boldsymbol{M_{HC}}$, (**b**) only the ring fault, $\boldsymbol{M_{RF}}$, and (**c**) only the ring fault, but excluding the two elements $M_{r\theta}$ and $M_{r\phi}$ (i.e., M_{rr}, $M_{\theta\theta}$, $M_{\phi\phi}$, and $M_{\theta\phi}$ of $\boldsymbol{M_{RF}}$). Note that the synthetic seismic waveforms are similar in all three cases, despite the differences in the moment tensors.

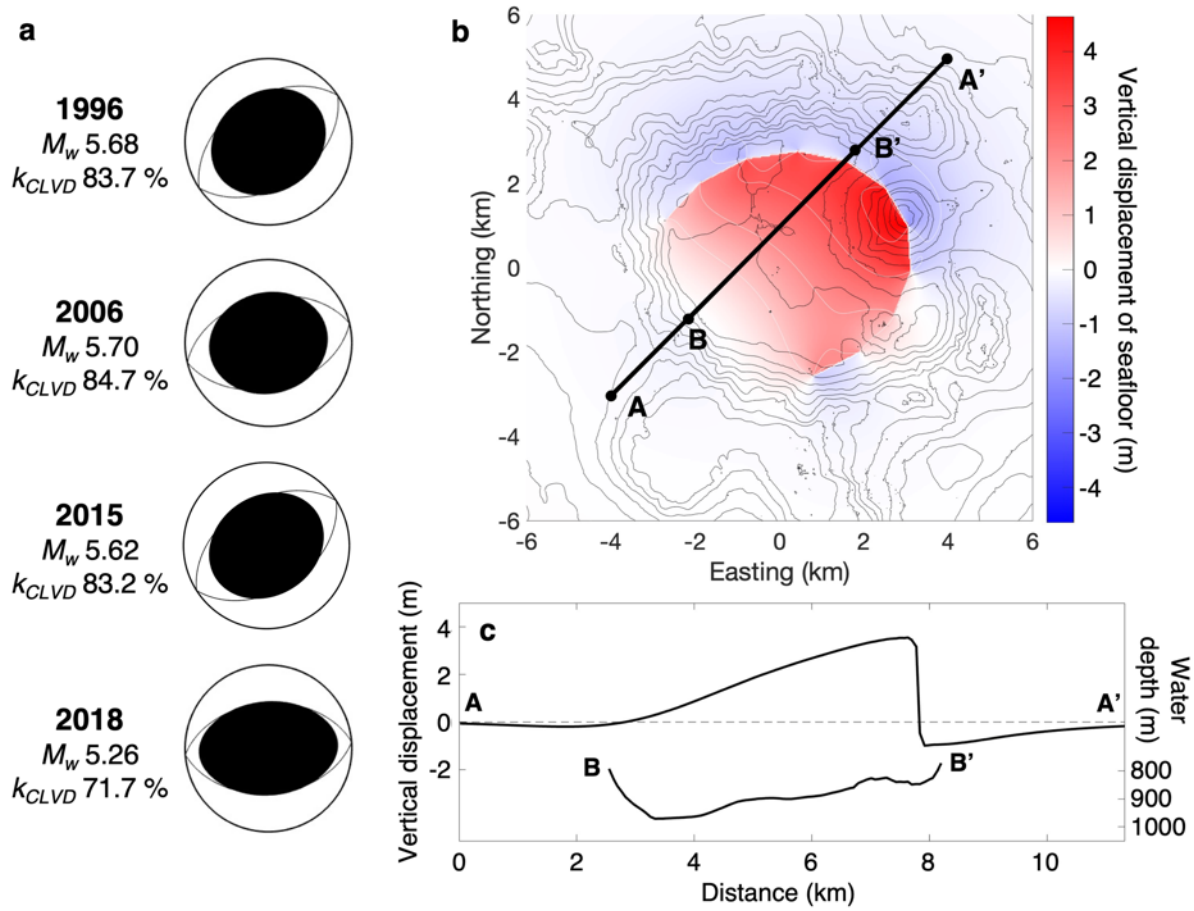

Figure 8. Recurrence of trapdoor faulting at Sumisu caldera. (**a**) Resolvable moment tensors $\boldsymbol{M_{res}}$ for the 1996, 2006, and 2015 earthquakes estimated by our moment tensor analysis. The orientation of the best double-couple solution is shown by thin curves. M_w and k_{CLVD} indicate the moment magnitude of $\boldsymbol{M_{res}}$ and the dominancy of the vertical-CLVD component in $\boldsymbol{M_{res}}$, respectively. (**b**) Vertical seafloor displacement computed with the best-fit source model for the 2015 earthquake (Figure 3b). (**c**) Profiles of the vertical seafloor displacement along A–A' shown in (**b**), and the topography along B–B'.